ATOLL GARNET: INSIGHTS FROM LA-ICP-MS TRACE ELEMENT MAPPING

Antoine Godet[1*], Tom Raimondo[2], Carl Guilmette[1]

1. E4m, Département de géologie et de génie géologique, Université Laval, Québec, Canada

2. UniSA STEM, University of South Australia, GPO Box 2471, Adelaide SA 5001, Australia

Abstract

Atoll garnets are uncommon features that have been recognized in contrasting metamorphic environments worldwide, but their origin remains largely debated. Several models have been proposed to explain their formation, including preferential dissolution of garnet cores by fluid infiltration, polymetamorphism, and the coalescence of subgrains. We report atoll-shaped garnets in an amphibolite-facies schist from the Paleoproterozoic New Quebec Orogen, Canada, and investigate their textural and chemical zoning through petrography, electron probe microanalysis (EPMA) and Laser Ablation Inductively Coupled Mass Spectrometry (LA-ICP-MS) maps. Textural evidence indicates a subhedral poikiloblastic core, an inclusion ring composed of matrix minerals, and a euhedral rim. Major element distribution maps show flat zoning, whereas trace elements show concentric growth zoning. Such characteristics are consistent with rapid, postkinematic growth involving Rayleigh fractionation of trace elements and coeval with accessory phase breakdown. Our observations rule out the preferential dissolution,

polymetamorphism and coalescence models, and support that the formation of atoll garnet in these rocks is best explained by a kinetic control and rapid growth. Our study concludes that the term “atoll” is more descriptive than genetic, and that the physio-chemical mechanisms leading to its formation should be assessed on a case-by-case basis using complementary tools, primarily including trace element mapping.

Keywords: Atoll garnet, trace element, zoning, mapping, LA-ICP-MS

Corresponding author: Antoine Godet, antoine.godet.1@ulaval.ca

Introduction

Atoll garnets are characterized by an island-core separated from a rim by a continuous annular-shaped mono-or polymineralic inclusion ring (Passchier and Trouw, 1998). They have been recognized in different localities worldwide and preserved in contrasting metamorphic environments, including (ultra) high pressure and eclogite contexts, contact aureoles, and Barrovian-like sequences. Well documented examples include the Dabie–Sulu HP-UHP metamorphic belt, China (Cao et al., 2018; Cheng et al., 2007; Cheng et al., 2009); Krusne Hory eclogites, Bohemian Massif (Faryad et al., 2010); UHP eclogites of the Tso Morari Complex, Himalaya (Jonnalagadda et al., 2017); Ardara pluton aureole, Ireland (Homam, 2003; Smellie, 1974); Ben Lui Schist, Scotland (Atherton and Edmunds, 1966); Apennine-Maghrebian orogen, Sicily (Ortolano et al., 2014); Sesia Zone, Italy (Robyr et al., 2014); Betic Belt, Spain (García-Casco and Torres-Roldán, 1996); Wakatipu Belt, New Zealand (Cooper, 1972); and Salvador–Esplanade Belt, Brazil (Goncalves et al., 2021), among others.

Several models and physio-chemical mechanisms have been proposed for the genesis of atoll garnet. A first model attributes the atoll shape to preferential dissolution of garnet cores over rims during fluid infiltration (Cheng et al., 2007; Faryad et al., 2010; Green, 1915; Jonnalagadda et al., 2017; Smellie, 1974). In this model, primary textural evidence is the presence of microveins and cracks, identified in-situ by back-scattered electron (BSE) imaging for example (e.g. Faryad et al., 2010; Jonnalagadda et al., 2017; Konrad-Schmolke et al., 2007), or resorbed garnet and hydrous phases inferred to result from garnet breakdown (e.g. Kulhánek et al., 2021). A second hypothesis is "pulsed" garnet growth attributed either to polymetamorphism or stoichiometric change of successive garnet-producing reactions separated by a hiatus (e.g. Cruz, 2011; Konrad-Schmolke et al., 2008a; Konrad-Schmolke et al., 2008b; Robyr et al., 2014). In this case, contrasting textural zones (i.e., core and rim) are expected to grow under contrasting *P-T* conditions and have a different chemical signature, as revealed by electron probe microanalysis (EPMA) for example. A third explanation involves multiple nucleation sites and the coalescence of subgrains (Cooper, 1972; Cruz, 2011; Spiess et al., 2001). Garnet in this instance is polycrystalline, as shown by electron backscatter diffraction (EBSD) analysis, and the atoll texture is attributed to fast nucleation of garnet aggregates in the rim preventing element mobility and diffusion toward the nucleation centre in the core. Finally, in a fourth model, the atoll texture is attributed to growth kinetics (Atherton and Edmunds, 1966), with rapid and short-term growth favourable to the development of a poikiloblastic texture. Overall, no consensus seems to emerge, and it is not clear whether the formation of atoll garnet derives from a uniformitarian single process, or from single or combined mechanisms that need to be addressed case-by-case.

Whereas textural relationships, crystallographic orientation, and major element content of atoll garnet are routinely investigated by BSE imaging (BSE, e.g. Cruz, 2011), EBSD analysis (EBSD, e.g. Spiess et al., 2001), and EMPA mapping (EPMA, e.g. Kulhánek et al., 2021; Robyr et al., 2014), respectively, the trace element distribution remains largely unassessed and limited to very few published studies (e.g. Goncalves et al., 2021; Kulhánek et al., 2021). This represents an open opportunity for new insights, given how useful trace elements are for deciphering garnet growth mechanisms, resorption, and diffusion processes (e.g. Konrad-Schmolke et al., 2008a; Raimondo et al., 2017; Rubatto et al., 2020; Skora et al., 2006). A growing number of studies demonstrate the benefits of Laser Ablation Inductively Coupled Mass Spectrometry (LA-ICP-MS) maps to evaluate trace element zoning (e.g. George et al., 2018; Godet et al., 2020a; Godet et al., 2020b; Guilmette et al., 2018; Raimondo et al., 2017; Rubatto et al., 2020), strengthening its emergence as the tool of choice to investigate garnet evolution.

Here, we investigate atoll garnet porphyroblasts from an amphibolite-facies schist of the New Quebec Orogen, Canada, using quantitative major element EPMA and trace element LA-ICP-MS mapping to discriminate between alternative hypotheses for its formation.

Geological background and sample petrography

The investigated specimen 3047A (584175-6284083, UTM nad83 zone 19; Godet et al., 2020b) was sampled in the New Quebec Orogen, located in northern Québec, Canada (Fig. 1a). This Paleoproterozoic accretionary orogen resulted from the collision of the eastern margin of the Archean Superior Craton, representing the lower plate of the

system, and the Kuujjuaq Domain, the Archean to Paleoproterozoic upper-plate (Henrique-Pinto et al., 2017; Wardle et al., 2002). The sample is derived from the metasedimentary Freneuse Suite (Simard et al., 2013) of the Rachel-Laporte Zone (Wardle et al., 2002). Quantitative petrochronological approaches and phase equilibria modeling have been used to date the burial of this supracrustal unit to middle-crust depths at *c*. 1795–1805 Ma (Lu-Hf on garnet and U-Pb on monazite dating, Godet et al., 2020b), and its metamorphic evolution along a clockwise metamorphic *P-T* path as part of an apparent Barrovian sequence with estimated peak conditions of 5–7 kbar and 620–650 °C.

Sample 3047A is a texturally homogeneous garnet-biotite schist (Fig. 1b, S1). The matrix (Fig. 1c) is composed of plagioclase (47 mode %), quartz (42 mode %) and biotite (8 mode %), with minor amounts of chlorite (0.2 mode %) and ilmenite (0.3 mode %; SEM-MLA scanning; Godet et al., 2020b). Accessory phases are zircon, rutile, monazite, apatite, and staurolite. Monazite, zircon, and apatite are observed in all garnet textural domains as well as in the matrix (Fig 1c, 2e, 2f). Rutile partially replaced by ilmenite occurs exclusively in the matrix (Fig 2g). Two preferential orientations of biotite define weak schistosity planes (Fig 1d). Subhedral atoll-shaped garnet porphyroblasts represent 1.6 mode % and are evenly distributed throughout the rock volume.

All garnet grains (1 to 3 mm in size) contain subhedral textural domains comprising a core, a polymineralic inclusion ring, and a rim (Fig 2 a-d; Fig. S1). Subhedral cores, representing ~30% of the garnet volume, have a poikiloblastic texture and contain variable amounts of relatively small monomineralic inclusions of matrix minerals, namely plagioclase, quartz, biotite and ilmenite. Polymineralic inclusion rings are evenly

distributed around cores and likewise contain matrix minerals with similar grain size. Biotite within the inclusion ring defines two preferential orientations parallel to the two schistosity plans observed in the matrix (Fig 1d, 2a, 2c). Subhedral to euhedral garnet rims (~70% of the garnet volume) contain fewer and generally coarser inclusions than the core and exhibit locally well-developed crystal faces on the outer sides (Fig 2 a-d). On the basis of inclusion abundances, rims can be further subdivided into a quartz-rich inner rim, and an inclusion-poor to inclusion-free outer rim (Fig 2 b, d). The core to rim relative volumes volumes vary from one porphyroblast to another, consistent with different latitudinal sections. Two atoll porphyroblasts inferred to represent equatorial sections – largest grains, largest cores, thinnest inclusion rings, and thinnest garnet rims - were selected for chemical analysis by EPMA and LA-ICP-MS.

Methods

EPMA

Mineral compositions were acquired on a Cameca SX-100 five-spectrometer electron probe micro-analyzer at the Département de géologie et génie géologique de l'Université Laval. Analytical conditions for spot analyses were 15 kV and 20 nA, with counting times of 20 s on peaks and 10 s on background. GEO standard block of P&H Developments were used to calibrate minerals, and Smithsonian microbeam standards Mineral Standard Mount MINM25-53 of Astimex Scientific Limited (Jarosewich et al., 1980) were used to calibrate oxides. Transects with an average of 15 to 20 spots were performed across garnet grains to quantify chemical zoning. Data were reduced using the PAP model (Pouchou and Pichoir, 1991). All oxides were converted in atom per formula unit (a.p.f.u) to get end-member compositions. End-member components of garnet used

in this study are $X_{Alm} = Fe^{2+}/(Fe^{2+}+ Mg+Ca+Mn)$; $X_{Grs} = Ca/(Ca+Fe^{2+}+Mg+Mn)$; $X_{Sps} = Mn/(Mn+Fe^{2+}+Mg+Ca)$; and $X_{Prp} = Mg/(Mg+Fe^{2+}+Ca+Mn)$. Major element maps (Fe, Mg, Ca, Mn) of whole or partial garnet grains were produced with a resolution of 512 by 512 pixels. Analytical conditions for whole grain analyses were 15 kV, 20 nA, and analysis time was 20 ms per pixel; analytical conditions for partial garnet grain analyses were 15 kV, 200 nA, and 100 ms per pixel.

LA-ICP-MS

Trace element zoning in garnet was mapped by Laser Ablation Inductively Coupled Plasma Mass Spectrometry (LA-ICP-MS). All maps were acquired using a Resonetics M-50-LR 193 nm excimer laser coupled to an Agilent 7700x Quadrupole ICP-MS housed at Adelaide Microscopy, University of Adelaide. Instrument conditions and mapping protocols are similar to those described in detail in Raimondo et al. (2017) and Hyppolito et al. (2018). Pre-ablation of each raster scan was completed to minimise the effect of redeposition (19 µm, 75% overlap), followed by 20 s washout and 15 s of background measurement. Ablation was performed in an atmosphere of UHP He (0.70 l/min), mixed with Ar (0.93 l/min) immediately after the ablation cell. A beam diameter of 16 µm, line spacing of 16 µm and repetition rate of 10 Hz were employed for all samples, resulting in an energy density of 3.5 J/cm^2 at the target. Standards were analysed in duplicate every 2 hours during the mapping session, including reference glasses NIST 610 and 612 (Jochum et al., 2011a; Pearce et al., 1997) and GSD-1D (Jochum et al., 2011b). A beam diameter of 51 µm was used for all standard spot analyses, and included 5 pre-ablation shots (51 µm, 75% overlap) followed by 20 s washout, 30 s background measurement

and 40 s ablation time. Data acquisition was performed in time-resolved analysis mode as a single continuous experiment. Data acquisition was performed in time-resolved analysis mode as a single continuous experiment. Each analysis comprised a suite of 32 elements, and dwell times were as follows: 0.002 (^{23}Na, ^{24}Mg, ^{27}Al, ^{29}Si, ^{31}P, ^{43}Ca, ^{55}Mn, ^{57}Fe), 0.005 (^{49}Ti, ^{51}V, ^{53}Cr, ^{178}Hf, ^{232}Th, ^{238}U), 0.008 (^{7}Li, ^{89}Y, ^{90}Zr, ^{139}La, ^{140}Ce, ^{141}Pr, ^{165}Ho, ^{166}Er, ^{169}Tm, ^{172}Yb, ^{175}Lu), 0.010 (^{88}Sr, ^{146}Nd, ^{159}Tb, ^{163}Dy), and 0.015 (^{147}Sm, ^{153}Eu, ^{157}Gd). The total sweep time was 0.280 s. Data were reduced in *Iolite* (Paton et al., 2011) following the procedure outlined in Raimondo et al. (2017), with quantification performed using ^{29}Si for internal calibration based on a weighted average of EPMA wt% SiO_2 values across each garnet grain. The Limit of Quantification (LOQ) of each element was calculated following Howell et al. (2013) and Raimondo et al. (2017). LOQ are provided as Supporting material Table S1. Background- and drift-corrected ppm data were then imported into *XMapTools* (Lanari et al., 2014; Raimondo et al., 2017) as a numerical matrix for image processing and manipulation.

Garnet major and trace element chemistry

The EPMA major element chemistry of two garnet porphyroblasts from sample 3047A is presented in Figures 3 and 4. Qualitative Fe, Mg, Ca, and Mn X-ray maps (Fig. 3) and quantitative spot transects of both grains (Fig. 4) exhibit homogeneous compositions from core to rim (X_{Alm} = 0.78–0.80; X_{Sps} = 0.01–0.02; X_{Prp} = 0.16–0.17; X_{Grs} = 0.02-0.03). Local compositional changes are observed in both garnet core and rim along some cracks – but not all of them (Fig 3, zoom 1) and in the immediate vicinity of inclusions (Fig 3, zoom 1; Fig. S2).

The trace element chemistry of one garnet porphyroblast was further investigated by LA-ICP-MS mapping. Selected quantitative maps and 1D line profiles are presented in Figures 5 and 6, respectively. All the garnet textural domains (i.e., core, inner rim and outer rim) show strong zoning in some trace elements. Approximately concentric zoning in Lu and Yb is observed (Fig 5), with the highest content at the centre of the core decreasing toward the outer rim, expressed as a bell-shaped distribution on the 1D profile (Fig 6a). In contrast, MREE, Y, Ho and Dy show a bowl-shaped distribution across the entire grain with a flat distribution across the core and the curvature localized at the inner- to outer-rim transition, and Er, and Tm show flat profiles (Fig 6b, c). Oscillatory zoning expressed by Dy and Ho is locally observed in garnet outer-rim (Fig. 5). Transition metal V is high in the entire rim with a drop in concentration towards the outer rim (Fig 6d). Chromium is patchier (Fig 5) and with higher content in the outer rim (Fig 5, 6c). LREE show flat profiles throughout the core, and comparatively low concentrations in the inner-rim and high concentrations in the outer-rim (Fig 6e). Higher Li content (>10 ppm) defines small linear features cross-cutting the zoning pattern defined by other trace elements, and oriented parallel to the schistosity planes defined by biotite inside and outside garnet (Fig 5).

The boundary between the inner and outer rim is markedly sharp in the V, Tb, Gd, Eu and Cr maps (Fig. 5), and is in all cases parallel to crystal faces. On a chondrite-normalized REE diagram (Fig 7), HREE content is progressively depleted from core to rim, and MREE content is correspondingly enriched. Most LREE do not show a clear pattern.

Quantitatively, Lu and Yb in the garnet core show highest values located at the centremost point (Lu ~5 ppm; Yb ~20 ppm), decreasing towards outer parts (Lu ~1 ppm; Yb ~10 ppm, Fig 6a). The inner rim is V-rich (~120 ppm), contains moderate amounts of Dy (~10–15 ppm), Tb (~1 ppm), Lu (~1.5 ppm) and Yb (~8–15 ppm), and shows low Eu (<0.2 ppm) and Cr (40–80 ppm) content (Fig 6b,c,d). The outer rim is enriched in Cr (up to 110 ppm), Gd (7 ppm), Tb (~3 ppm) and Sm (~0.5 ppm) relative to the core and inner rim (Fig 6c,e). Both the inner and outer rims are enriched in Ti (15–40 ppm) compared to core (5–10 ppm, Fig 6d).

Discussion

Here, textural evidence coupled with major and trace element distributions are discussed to test the different mechanisms proposed for the nucleation and growth of atoll garnet, namely pulsed growth during polymetamorphism (e.g. Robyr et al., 2014), preferential dissolution (e.g. Faryad et al., 2010; Smellie, 1974), multiple nucleation centres (Cooper, 1972; Spiess et al., 2001) and growth kinetics (Atherton and Edmunds, 1966).

Textural evidence

Garnet porphyroblasts in sample 3047A are approximately uniform in size, show the same regular atoll habit, and are evenly distributed throughout the rock volume (Fig. 2). As opposed to other examples where atoll shapes are confined to specific grains (e.g. Cheng et al., 2007) or layers (e.g. Faryad et al., 2010), this observation is consistent with a ubiquitous mechanism for their formation in our sample. All garnet grains

systematically contain the same subdomains of a subhedral poikiloblastic core, an inclusion ring, an inclusion-rich inner rim and an inclusion-poor outer rim (Figure 1c-d, 2a-d). Both the poikiloblastic core and the polymineralic inclusion ring are characterized by plagioclase, quartz, biotite, and ilmenite assemblage in all aspects similar to the matrix assemblage. Remarkably, the orientation of biotite within the garnet core, inclusion ring, and garnet rim is parallel to the preferred orientation in the surrounding matrix (Fig 1c-d, 2a, 2c). This strongly supports that garnet was superimposed on the schistosity and implies a post-kinematic nucleation and growth of at least the inner and outer rim domains. The preservation of quartzo-feldspathic matrix-assemblage and matrix-parallel oriented fabric inside the inclusion ring rules out preferential core and/or mantle dissolution by fluid infiltration, which involves post-kinematic retrogression and replacement by hydrous assemblage differing from the matrix, as described by Cheng et al. (2007); Faryad et al. (2010); Smellie (1974), among others.

Major element distribution

The two investigated garnet porphyroblasts have almost identical chemistries, which we consider representative of the tens of grains in the investigated thin section as observed during SEM-MLA particle classification (Fig. 1). The two grains feature overall homogeneous distributions of major elements (Fig. 3). The homogeneous elemental distribution of Ca, Fe, Mg, and Mn is explained either by the absence of any initial growth zoning, or homogenization through intracrystalline diffusion at amphibolite facies (e.g. Caddick et al., 2010; Spear, 1991). Possible explanations for the absence of initial growth zoning are that garnet growth occurred in a tight *P-T* window without chemical

changes to the matrix in the immediate vicinity of garnet nuclei; that elemental transport to the advancing interface was limited; and/or that fast kinetic processes operated throughout the growth history (e.g. Carlson, 2011).

Growth within a tight *P-T* window was assessed by contouring the *P-T* pseudosection calculated by Godet et al. (2020b) for isomodes and isopleths using TCInvestigator software (Pearce et al., 2015). The method is provided as supporting material (Appendix 1) and the results are presented in Figures 8 & 9. Garnet isomodes are parallel to the garnet-in reaction and increase from 0 to ~2 mode% with increasing temperature from ~575 to 675 °C. Compositional garnet isopleths show variations in the *P-T* window of interest (~575–625 °C; 4–7 kbar), with Fe# ($x(Grt)=Fe^{2+}/(Fe^{2+}+Mg^{2+})$) content - parallel to garnet isomodes - decreasing from 0.85 to 0.78 as temperature increases, and XCa ($z(Grt) = Ca^{2+}/(Ca^{2+}+Fe^{2+}+Mg^{2+})$) content slightly increasing (0.02 to 0.03) with increasing pressure and temperature. Except for the unlikely scenario of isothermal burial, no tight *P-T* window with homogeneous composition is therefore predicted during garnet growth (i.e. crossing isomodes), ruling out a *P-T* control on the distribution of major elements.

The alternative hypothesis of limited nutrient transport (e.g. Carlson, 2011) is likewise considered doubtful because (1) the rock is texturally homogeneous and only shows a weak structural fabric -by opposition to a layered or gneissic rock volume preventing distributed nutrient transport; (2) water was considered to be in excess; and (3) trace elements define sharp zoning suggesting fast uptake of elements liberated by accessory phase breakdown (see below). This leaves the conclusion that nutrient transport was not a

limiting factor and that garnet growth benefited from rapid diffusion in a spatially uniform nutrient reservoir (Carlson, 2011).

On the other hand, the major element distribution is better explained by homogenization through intracrystalline diffusion under amphibolite facies conditions (e.g. Caddick et al., 2010; Spear, 1991). While the modal proportions of the major phases (i.e. Grt, Bt, Pl, Chl) are successfully modelled in the field of interest and intersect with the relatively immobile Ca content of garnet (Vielzeuf et al., 2007), the isopleths predicted for the ferromagnesian endmembers remain at odds with observations. Using empirical thermometry and modelling the structural water bulk composition, Godet et al. (2020b) argued that the Fe-Mg content of garnet and biotite was affected by diffusion upon cooling. The thermal resetting and homogeneous distribution of the major elements is therefore interpreted as resulting from post-metamorphic peak conditions and could be excluded from the list of potential controlling factor in the development of the atoll shape.

Trace element distribution

Compared to major elements, garnet trace element zoning is far more resilient to resetting due to the lower diffusion coefficients of trivalent cations (Kohn, 2009), commonly leading to their decoupling (Kotková and Harley, 2010; Moore et al., 2013; Raimondo et al., 2017). Several factors controlling trace element incorporation and distribution in garnet have been identified, including (1) resorption (or recrystallization); (2) breakdown of a trace element-bearing major or accessory phase during garnet growth; (3) change in

292 the kinetics of garnet growth; (4) overprint zoning; (5) intracrystalline diffusion; and (6)
293 infiltration of trace element-rich fluid (e.g. Baxter et al., 2017; Carlson, 2012; Konrad-
294 Schmolke et al., 2008a; Pyle and Spear, 1999; Skora et al., 2006).

295 The presence of crystal-face parallel zoning observed between the inner and outer rim in
296 sample 3047A, and local oscillatory zoning (Fig. 5) support that growth zoning is
297 preserved at least in the rim, ruling out any control by resorption, or overprinting, and
298 consistent with limited intracrystalline diffusion. The analysed grain features concentric
299 zoning in Lu, Yb and Tm, with highest values located in the core and decreasing
300 rimward. This reflects progressive garnet uptake and corresponding depletion of the
301 matrix reservoir, and is attributed to Rayleigh fractionation (Hollister, 1966). We note
302 that the absence of annular maxima does not fit the model of diffusion-limited uptake of
303 trace elements (Moore et al., 2013; Skora et al., 2006). It also argues against any open
304 system behaviour or bulk modification by HREE-rich fluid infiltration during garnet
305 growth.

306 Some trace elements (including V, Cr, Eu, Gd, Tb and Dy; Figs 5 and 6) exhibit
307 concentric zoning with a discrete transition marking the boundary between the inner and
308 outer rims. This observation is inconsistent with the hypothesis of multiple nucleation
309 and coalescence proposed for the development of atoll garnet (Spiess et al. 2001) but
310 would benefit from EBSD analysis (Whitney and Seaton, 2010). The absence of trace
311 elements redistribution following garnet breakdown (e.g. back-retreat processes) is also
312 inconsistent with polymetamorphism as a control on the atoll shape, an inference that
313 concurs with the absence of multiple metamorphic events identified in the
314 geochronological record of both this sample and the Rachel-Laporte Zone as a whole

(Godet et al., 2020b). We thus infer that element availability was mainly controlled by major and accessory phases growth and breakdown.

Compared to the core and outer rim, the inner rim is enriched in V and Ti (Figure 5). We infer that this enrichment is due to the breakdown of rutile, which may incorporate both of these elements in its crystalline structure (Zack et al., 2002), with a likely contribution of white micas breakdown (Yang and Rivers, 2000). This rutile to ilmenite transition is predicted at higher pressure by phase equilibria modeling (Godet et al., 2020b) and observed in thin section (Figure 2g). The location of this transition in a P-T space is highly dependent on fO_2 during prograde metamorphism, which is notoriously difficult to constrain. Godet et al. (2020b) fixed an arbitrary Fe^{3+}/Fe_{Tot} ratio (O = 0.05), but an even lower ratio is reasonable, which would favor rutile stability over ilmenite and move the rutile to ilmenite transition towards the field of observed assemblage. The pseudosection also predicts a white-mica-out isograd reaction that actually constrains the tield of observed assemblage at higher P – lower T (Fig. 8).

The outer rim is similarly enriched in Cr, Y, LREE and MREE (Figures 5-7), which we attribute to allanite breakdown. The allanite-to-monazite reaction, common for such bulk compositions, is mainly *T*-dependent and broadly occurs at the garnet-in or staurolite-in isograd reactions (Kingsbury et al., 1993; Rubatto et al., 2001; Smith and Barreiro, 1990), with several studies invoking this mechanism to explain trace element uptake in garnet (e.g. Boston et al., 2017; Gieré et al., 2011; Rubatto et al., 2020). This hypothesis is consistent with prograde subsolidus monazite identified from sample 3047A, which returns an age similar to garnet growth ages in the same lithotectonic zone (Godet et al., 2020b).

High Li content defines linear features, parallel to apparent microfractures or not (Fig. 5). They are mostly observed in the garnet rim as cross cutting the zoning pattern of other trace elements (Fig 5), and define two preferred orientations parallel to the two fabrics marked by biotite in matrix and as inclusion within garnet. This relationship suggests overprinting zoning inherited from a prior matrix distribution of Li, mainly hosted by biotite, implying that Li remained immobile and further supporting post-kinematic garnet rim growth. Similar inherited or remnant zoning has previously been described for Cr for example (e.g. Raimondo et al., 2017; Yang and Rivers, 2001), however, the reasons for relative Li immobility remain unclear.

Potential kinetic control on the development atoll garnet

In summary, the textural and major and trace element arguments explored above lead to the following conclusions: (i) the matrix mineral assemblage preserved in the atoll ring rules out its formation by dissolution during fluid infiltration; (ii) the protracted predicted growth zoning and the absence of garnet consumption; as well as the geochronological record of the region are inconsistent with polymetamorphism; and (iii) concentric trace element zoning was controlled by Rayleigh fractionation in the core, and by the breakdown of accessory phases (rutile and allanite) in the rim, are consistent with growth around a single nuclei, and inconsistent with the hypothesis of multiple nucleation centres. An alternative explanation for atoll garnet formation in our sample is that a switch in the controlling mechanisms during garnet growth explains the development of the atoll shape. However, such switching has also been described in “non atoll-shaped” garnet (e.g. George et al., 2018), and is therefore not a discriminating growth model.

Hereafter, we use phase equilibria modeling to explore chemical and mineral assemblage changes during garnet growth and explore how the remaining hypothesis of kinetic processes may have contributed to the development of atoll garnet.

Our phase equilibria modeling approach enables to further investigate chemical and mineralogical changes during garnet growth (e.g. Konrad-Schmolke et al., 2008a). As mentioned above, Godet et al. (2020b) identified intra- and inter-crystalline diffusion as having exerted a strong control on Fe, Mg, and Mn. We will accordingly focus our analysis on modal proportions, which were not affected by diffusion reactions, and on Ca isopleths, a slow diffusing cation that potentially preserved some prograde information (Vielzeuf et al., 2007). A hypothetical prograde P-T path is divided in segments as follows (Fig. 9). Step 1, starting at the garnet-in isograd reaction, illustrates the nucleation and growth of the poikiloblastic garnet core (about 30 vol%) in a homogeneous matrix without any major change of the surrounding mineral assemblage and low relative free water production rate (dH_2O/dT). This segment is parallel to grossular isopleth (z(g)) and predicts a homogeneous Ca content in the core domain as observed (Figs. 3 & 4; Table S2). Step 2 corresponds to the staurolite-in and paragonite-out reactions in a tight P-T window, associated with a major change of the matrix mineral assemblage including devolatilization and release of free water in the system. This segment is also sub-parallel to garnet isomodes consistent with an interruption of garnet growth. Finally, Step 3 illustrates the efficient growth of garnet rim (~70 vol%) boosted by a higher free water production rate and higher temperature conditions and resulting in euhedral to subhedral shape. The relatively big size of the inclusions in the inner-rim relative to inclusions in the core is also consistent with the coarser grain size of the matrix

toward high temperature during step 3. Overall, while the exact mechanism for the formation of the atoll-shape is still unclear, phase equilibria modeling adequately predicts apparent major chemical, textural, and mineralogical changes between garnet core and garnet rim domains with increase of the free water content that may have played an important role.

In a chemically homogeneous mineral assemblage, nucleation and growth are dictated by cation diffusion range and rate. Such parameters can influence grain size and shape (e.g. Atherton and Edmunds, 1966; Carlson, 2011; George and Gaidies, 2017). Due to the exponential response of crystallization rate to thermal increase, and because nucleation rates may vary markedly in time and space during crystallization (Kelly et al., 2013), the most fundamental control on the rate of prograde metamorphism is simply the rate of temperature increase (Carlson, 2011). Thus, we tentatively propose that the atoll garnet texture resulted from a rapid garnet rim growth following a rapid temperature increase and high cation diffusion rate favoured by free water release (step 2 on Fig. 9). The poikiloblastic texture observed in the garnet inner rim is consistent with rapid and short-term growth (Atherton and Edmunds, 1966). This likely produced the simultaneous growth of numerous similarly-sized rim domains overgrowing prograde garnet-zone core cores following a hiatus in garnet growth at the white mica-out and staurolite-in boundaries. Alternative approaches such as geospeedometry and cation diffusion modelling could thus be relevant to fully explore the nucleation and growth mechanisms of atoll garnet (George and Gaidies, 2017).

Conclusion

"Atoll garnet" is an expression that has been broadly used in different contexts, generally to describe garnet characterized by an island-core separated from a rim by an inclusion ring, or by an annular shape with no proper core. It is a descriptive rather than a genetic term, and may encapsulate wide range of textural diversity. The kinetic control and rapid growth hypothesis we prefer here for garnet formation is therefore not necessarily applicable to all atoll garnets, depending on the specific texture or set of relationships that are being considered. As such, our trace element arguments should not be taken in isolation, but rather add the final revealing details to growth processes that may be cryptically or incompletely recorded by other textural, mineralogical, geochemical and/or *P-T* modelling evidence. This integrated approach represents the best means to build a complete picture of the garnet nucleation and growth history, and thereby discriminate between the various hypothesis proposed.

Acknowledgements

This research was financially supported by NSERC (DG RGPIN-2020-06400 attributed to CG) and the MERN (#8449 – 2021-2022 – 03). Marc Choquette is thanked for his help during analytical acquisition. Loic Labrousse is thanked for fruitful discussion. We acknowledge Matthias Konrad-Schmolke and Freya George for their constructive comments that helped improve this manuscript. Daniela Rubatto is acknowledged for her useful suggestions and editorial handling.

References

Atherton, M., and Edmunds, W., 1966, An electron microprobe study of some zoned garnets from metamorphic rocks: Earth and Planetary Science Letters, v. 1, no. 4, p. 185-193.

Baxter, E., Caddick, M., and Dragovic, B., 2017, Garnet: A rock-forming mineral petrochronometer: Reviews in Mineralogy and Geochemistry, v. 83, no. 1, p. 469-533.

Boston, K. R., Rubatto, D., Hermann, J., Engi, M., and Amelin, Y., 2017, Geochronology of accessory allanite and monazite in the Barrovian metamorphic sequence of the Central Alps, Switzerland: Lithos, v. 286, p. 502-518.

Caddick, M. J., Konopasek, J., and Thompson, A. B., 2010, Preservation of Garnet Growth Zoning and the Duration of Prograde Metamorphism: Journal of Petrology, v. 51, no. 11, p. 2327-2347.

Cao, D., Cheng, H., Zhang, L., and Wang, K., 2018, Origin of atoll garnets in ultra-high-pressure eclogites and implications for infiltration of external fluids: Journal of Asian Earth Sciences, v. 160, p. 224-238.

Carlson, W. D., 2011, Porphyroblast crystallization: linking processes, kinetics, and microstructures: International Geology Review, v. 53, no. 3-4, p. 406-445.

Carlson, W. D., 2012, Rates and mechanism of Y, REE, and Cr diffusion in garnet: American Mineralogist, v. 97, no. 10, p. 1598-1618.

Cheng, H., Nakamura, E., Kobayashi, K., and Zhou, Z., 2007, Origin of atoll garnets in eclogites and implications for the redistribution of trace elements during slab exhumation in a continental subduction zone: American Mineralogist, v. 92, no. 7, p. 1119-1129.

Cheng, H., Nakamura, E., and Zhou, Z., 2009, Garnet Lu–Hf dating of retrograde fluid activity during ultrahigh-pressure metamorphic eclogites exhumation: Mineralogy and Petrology, v. 95, no. 3-4, p. 315-326.

Cooper, A., 1972, Progressive metamorphism of metabasic rocks from the Haast Schist Group of southern New Zealand: Journal of petrology, v. 13, no. 3, p. 457-492.

Cruz, M. D. R., 2011, Origin of atoll garnet in schists from the Alpujárride Complex (Central zone of the Betic Cordillera, Spain): implications on the PT evolution: Mineralogy and Petrology, v. 101, no. 3-4, p. 245-261.

Faryad, S., Klápová, H., and Nosál, L., 2010, Mechanism of formation of atoll garnet during high-pressure metamorphism: Mineralogical Magazine, v. 74, no. 1, p. 111-126.

García-Casco, A., and Torres-Roldán, R. L., 1996, Disequilibrium Induced by Fast Decompression in St− Bt− Grt− Ky− Sil− And Metapelites from the Betic Belt (Southern Spain): Journal of Petrology, v. 37, no. 5, p. 1207-1239.

George, F., and Gaidies, F., 2017, Characterisation of a garnet population from the Sikkim Himalaya: insights into the rates and mechanisms of porphyroblast crystallisation: Contributions to Mineralogy and Petrology, v. 172, no. 7, p. 1-22.

George, F., Gaidies, F., and Boucher, B., 2018, Population-wide garnet growth zoning revealed by LA-ICP-MS mapping: implications for trace element equilibration and syn-kinematic deformation during crystallisation: Contributions to Mineralogy and Petrology, v. 173, no. 9, p. 1-22.

Gieré, R., Rumble, D., Günther, D., Connolly, J., and Caddick, M. J., 2011, Correlation of growth and breakdown of major and accessory minerals in metapelites from Campolungo, Central Alps: Journal of Petrology, v. 52, no. 12, p. 2293-2334.

Godet, A., Guilmette, C., Labrousse, L., Davis, D. W., Smit, M. A., Cutts, J. A., Vanier, M. A., Lafrance, I., and Charette, B., 2020a, Complete metamorphic cycle and long-lived

anatexis in the c. 2.1 Ga Mistinibi Complex, Canada: Journal of Metamorphic Geology, v. 38, no. 3, p. 235-264.
Godet, A., Guilmette, C., Labrousse, L., Smit, M. A., Davis, D. W., Raimondo, T., Vanier, M.-A., Charette, B., and Lafrance, I., 2020b, Contrasting P-T-t paths reveal a metamorphic discontinuity in the New Quebec Orogen: Insights into Paleoproterozoic orogenic processes: Precambrian Research, v. 342, no. 14.
Goncalves, P., Raimondo, T., Paquette, J. L., and Santos de Souza de Oliveira, J., 2021, Garnet as a monitor for melt–rock interaction: Textural, mineralogical, and compositional evidence of partial melting and melt-driven metasomatism: Journal of Metamorphic Geology.
Green, J. F. N., 1915, The garnets and streaky rocks of the English Lake District: Mineralogical magazine and journal of the Mineralogical Society, v. 17, no. 81, p. 207-217.
Guilmette, C., Smit, M. A., van Hinsbergen, D. J., Gürer, D., Corfu, F., Charette, B., Maffione, M., Rabeau, O., and Savard, D., 2018, Forced subduction initiation recorded in the sole and crust of the Semail Ophiolite of Oman: Nature Geoscience, v. 11, no. 9, p. 688.
Henrique-Pinto, R., Guilmette, C., Bilodeau, C., and McNicoll, V., 2017, Evidence for transition from a continental forearc to a collisional pro-foreland basin in the eastern Trans-Hudson Orogen: Detrital zircon provenance analysis in the Labrador Trough, Canada: Precambrian Research, v. 296, p. 181-194.
Hollister, L. S., 1966, Garnet zoning: an interpretation based on the Rayleigh fractionation model: Science, v. 154, no. 3757, p. 1647-1651.
Homam, S. M., 2003, Formation of atoll garnet in the Ardara Aureole, NW Ireland.
Howell, D., Griffin, W., Pearson, N., Powell, W., Wieland, P., and O'Reilly, S., 2013, Trace element partitioning in mixed-habit diamonds: Chemical Geology, v. 355, p. 134-143.
Hyppolito, T., Cambeses, A., Angiboust, S., Raimondo, T., García-Casco, A., and Juliani, C., 2018, Rehydration of eclogites and garnet-replacement processes during exhumation in the amphibolite facies: Geological Society, London, Special Publications, v. 478, p. SP478. 473.
Jarosewich, E., Nelen, J., and Norberg, J. A., 1980, Reference samples for electron microprobe analysis: Geostandards and Geoanalytical Research, v. 4, no. 1, p. 43-47.
Jochum, K. P., Weis, U., Stoll, B., Kuzmin, D., Yang, Q., Raczek, I., Jacob, D. E., Stracke, A., Birbaum, K., and Frick, D. A., 2011a, Determination of reference values for NIST SRM 610–617 glasses following ISO guidelines: Geostandards and Geoanalytical Research, v. 35, no. 4, p. 397-429.
Jochum, K. P., Wilson, S. A., Abouchami, W., Amini, M., Chmeleff, J., Eisenhauer, A., Hegner, E., Iaccheri, L. M., Kieffer, B., and Krause, J., 2011b, GSD-1G and MPI-DING reference glasses for in situ and bulk isotopic determination: Geostandards and Geoanalytical Research, v. 35, no. 2, p. 193-226.
Jonnalagadda, M. K., Karmalkar, N. R., Duraiswami, R. A., Harshe, S., Gain, S., and Griffin, W. L., 2017, Formation of atoll garnets in the UHP eclogites of the Tso Morari Complex, Ladakh, Himalaya: Journal of Earth System Science, v. 126, no. 8, p. 1-23.
Kelly, E., Carlson, W., and Ketcham, R., 2013, Crystallization kinetics during regional metamorphism of porphyroblastic rocks: Journal of Metamorphic Geology, v. 31, no. 9, p. 963-979.
Kingsbury, J. A., Miller, C. F., Wooden, J. L., and Harrison, T. M., 1993, Monazite paragenesis and U-Pb systematics in rocks of the eastern Mojave Desert, California, USA: implications for thermochronometry: Chemical Geology, v. 110, no. 1-3, p. 147-167.

Konrad-Schmolke, M., O'Brien, P. J., de Capitani, C., and Carswell, D. A., 2008a, Garnet growth at high-and ultra-high pressure conditions and the effect of element fractionation on mineral modes and composition: Lithos, v. 103, no. 3-4, p. 309-332.

Konrad-Schmolke, M., O'Brien, P. J., and Heidelbach, F., 2007, Compositional re-equilibration of garnet: the importance of sub-grain boundaries: European Journal of Mineralogy, v. 19, no. 4, p. 431-438.

Konrad-Schmolke, M., Zack, T., O'Brien, P. J., and Jacob, D. E., 2008b, Combined thermodynamic and rare earth element modelling of garnet growth during subduction: examples from ultrahigh-pressure eclogite of the Western Gneiss Region, Norway: Earth and Planetary Science Letters, v. 272, no. 1-2, p. 488-498.

Kotková, J., and Harley, S. L., 2010, Anatexis during high-pressure crustal metamorphism: evidence from garnet–whole-rock REE relationships and zircon–rutile Ti–Zr thermometry in leucogranulites from the Bohemian Massif: Journal of Petrology, v. 51, no. 10, p. 1967-2001.

Kulhánek, J., Faryad, S. W., Jedlicka, R., and Svojtka, M., 2021, Dissolution and Reprecipitation of Garnet during Eclogite-facies Metamorphism; Major and Trace Element Transfer during Atoll Garnet Formation: Journal of Petrology, v. 62, no. 11, p. egab077.

Lanari, P., Vidal, O., De Andrade, V., Dubacq, B., Lewin, E., Grosch, E. G., and Schwartz, S., 2014, XMapTools: A MATLAB©-based program for electron microprobe X-ray image processing and geothermobarometry: Computers & Geosciences, v. 62, p. 227-240.

Moore, S., Carlson, W., and Hesse, M., 2013, Origins of yttrium and rare earth element distributions in metamorphic garnet: Journal of Metamorphic Geology, v. 31, no. 6, p. 663-689.

Ortolano, G., Visalli, R., Cirrincione, R., and Rebay, G., 2014, PT-path reconstruction via unraveling of peculiar zoning pattern in atoll shaped garnets via image assisted analysis: an example from the Santa Lucia del Mela garnet micaschists (northeastern Sicily-Italy): Periodico di Mineralogia, v. 83, no. 2, p. 257-297.

Passchier, C., and Trouw, R., 1998, Deformation mechanisms, Microtectonics, Springer, p. 25-56.

Paton, C., Hellstrom, J., Paul, B., Woodhead, J., and Hergt, J., 2011, Iolite: Freeware for the visualisation and processing of mass spectrometric data: Journal of Analytical Atomic Spectrometry, v. 26, no. 12, p. 2508-2518.

Pearce, M. A., White, A. J. R., and Gazley, M. F., 2015, TCInvestigator: automated calculation of mineral mode and composition contours for thermocalc pseudosections: Journal of Metamorphic Geology, v. 33, no. 4, p. 413-425.

Pearce, N. J., Perkins, W. T., Westgate, J. A., Gorton, M. P., Jackson, S. E., Neal, C. R., and Chenery, S. P., 1997, A compilation of new and published major and trace element data for NIST SRM 610 and NIST SRM 612 glass reference materials: Geostandards Newsletter, v. 21, no. 1, p. 115-144.

Pouchou, J.-L., and Pichoir, F., 1991, Quantitative analysis of homogeneous or stratified microvolumes applying the model "PAP", Electron probe quantitation, Springer, p. 31-75.

Pyle, J. M., and Spear, F. S., 1999, Yttrium zoning in garnet: coupling of major and accessory phases during metamorphic reactions: Geological Materials Research, v. 1, no. 6, p. 1-49.

Raimondo, T., Payne, J., Wade, B., Lanari, P., Clark, C., and Hand, M., 2017, Trace element mapping by LA-ICP-MS: assessing geochemical mobility in garnet: Contributions to Mineralogy and Petrology, v. 172, no. 4, p. 17.

568 Robyr, M., Darbellay, B., and Baumgartner, L., 2014, Matrix-dependent garnet growth in
569 polymetamorphic rocks of the Sesia zone, Italian Alps: Journal of metamorphic geology,
570 v. 32, no. 1, p. 3-24.
571 Rubatto, D., Burger, M., Lanari, P., Hattendorf, B., Schwarz, G., Neff, C., Keresztes Schmidt, P.,
572 Hermann, J., Vho, A., and Günther, D., 2020, Identification of growth mechanisms in
573 metamorphic garnet by high-resolution trace element mapping with LA-ICP-TOFMS:
574 Contributions to mineralogy and petrology, v. 175, p. 1-19.
575 Rubatto, D., Williams, I. S., and Buick, I. S., 2001, Zircon and monazite response to prograde
576 metamorphism in the Reynolds Range, central Australia: Contributions to Mineralogy
577 and Petrology, v. 140, no. 4, p. 458-468.
578 Simard, M., Lafrance, I., Hammouche, H., and Legouix, C., 2013, Géologie de la région de
579 Kuujjuaq et de la Baie d'Ungava (SNRC 24J et 24K): Ministère des Ressources naturelles,
580 Québec;, v. RG 2013-04, p. 60 pages.
581 Skora, S., Baumgartner, L. P., Mahlen, N. J., Johnson, C. M., Pilet, S., and Hellebrand, E., 2006,
582 Diffusion-limited REE uptake by eclogite garnets and its consequences for Lu–Hf and
583 Sm–Nd geochronology: Contributions to Mineralogy and Petrology, v. 152, no. 6, p. 703-
584 720.
585 Smellie, J., 1974, Formation of atoll garnets from the aureole of the Ardara pluton, Co. Donegal,
586 Ireland: Mineralogical magazine, v. 39, no. 308, p. 878-888.
587 Smith, H. A., and Barreiro, B., 1990, Monazite U-Pb dating of staurolite grade metamorphism in
588 pelitic schists: Contributions to Mineralogy and Petrology, v. 105, no. 5, p. 602-615.
589 Spear, F. S., 1991, On the interpretation of peak metamorphic temperatures in light of garnet
590 diffusion during cooling: Journal of Metamorphic Geology, v. 9, no. 4, p. 379-388.
591 Spiess, R., Peruzzo, L., Prior, D., and Wheeler, J., 2001, Development of garnet porphyroblasts by
592 multiple nucleation, coalescence and boundary misorientation-driven rotations: Journal
593 of Metamorphic Geology, v. 19, no. 3, p. 269-290.
594 Taylor, S., and McClennan, S., 1985, The continental crustal: its composition and evolution.:
595 Blackwell, Oxford, p. 312.
596 Vielzeuf, D., Baronnet, A., Perchuk, A., Laporte, D., and Baker, M., 2007, Calcium diffusivity in
597 alumino-silicate garnets: an experimental and ATEM study: Contributions to Mineralogy
598 and Petrology, v. 154, no. 2, p. 153-170.
599 Wardle, R. J., James, D. T., Scott, D. J., and Hall, J., 2002, The southeastern Churchill Province:
600 synthesis of a Paleoproterozoic transpressional orogen: Canadian Journal of Earth
601 Sciences, v. 39, no. 5, p. 639-663.
602 Whitney, D. L., and Seaton, N. C., 2010, Garnet polycrystals and the significance of clustered
603 crystallization: Contributions to Mineralogy and Petrology, v. 160, no. 4, p. 591-607.
604 Yang, P., and Rivers, T., 2000, Trace element partitioning between coexisting biotite and
605 muscovite from metamorphic rocks, Western Labrador: Structural, compositional and
606 thermal controls: Geochimica et Cosmochimica Acta, v. 64, no. 8, p. 1451-1472.
607 -, 2001, Chromium and manganese zoning in pelitic garnet and kyanite: Spiral, overprint, and
608 oscillatory (?) zoning patterns and the role of growth rate: Journal of Metamorphic
609 Geology, v. 19, no. 4, p. 455-474.
610 Zack, T., Kronz, A., Foley, S. F., and Rivers, T., 2002, Trace element abundances in rutiles from
611 eclogites and associated garnet mica schists: Chemical Geology, v. 184, no. 1-2, p. 97-
612 122.

Figure captions

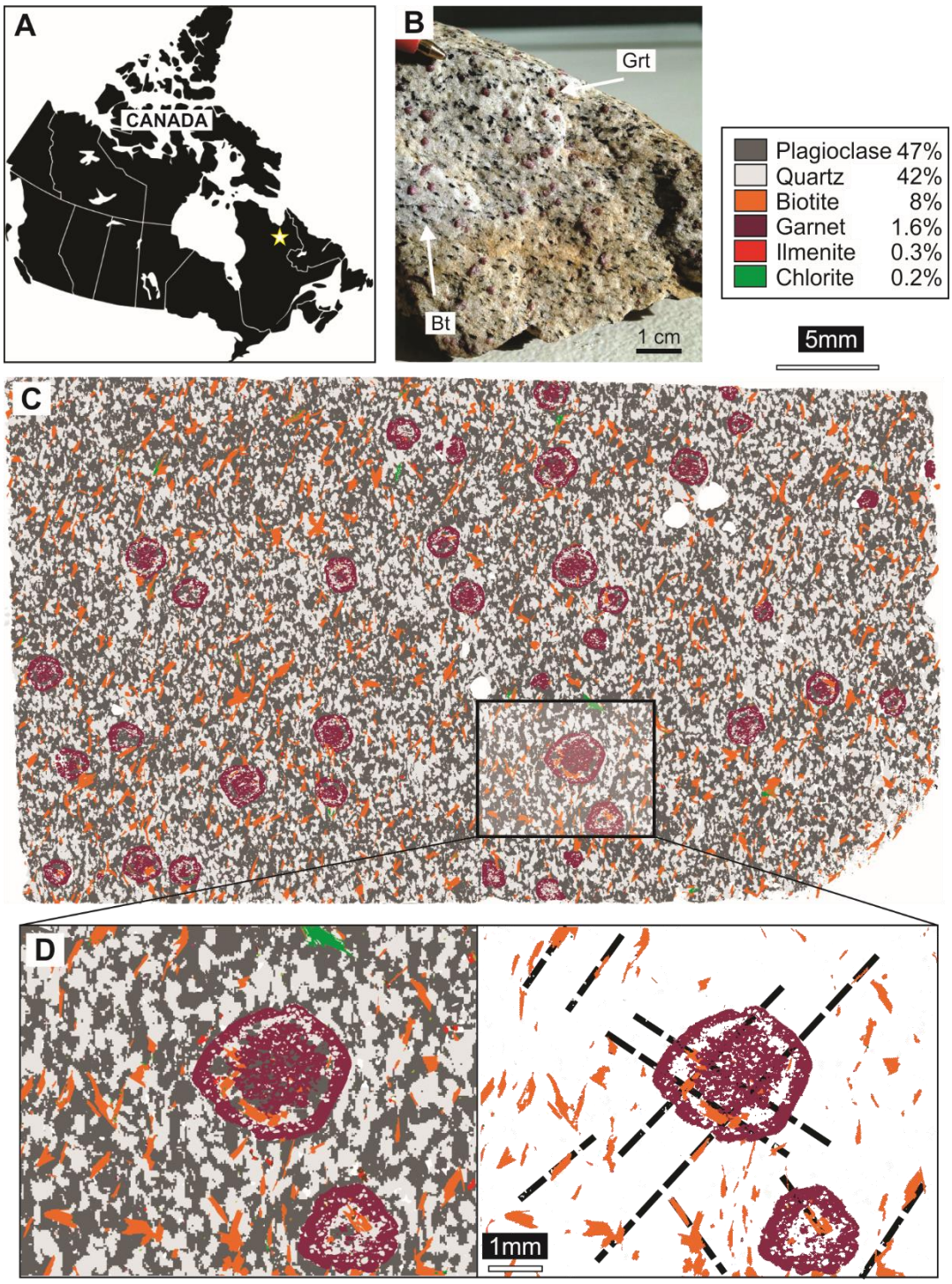

Figure 1. (a) Sample location within the New Quebec Orogen, indicated by the yellow star. Coordinates are provided in text; (b) Photograph of the texturally homogeneous hand sample; (c) False-color scanning electron microscope–mineral liberation analysis (SEM-MLA) map of the investigated thin section (modified from Godet et al., 2020b). Modal proportions of rock-forming minerals are provided in the legend. (d) zoom and interpretation drawing showing the two preferential orientations of biotite (black dashed lines). Abbreviations: Bt = biotite; Grt = garnet.

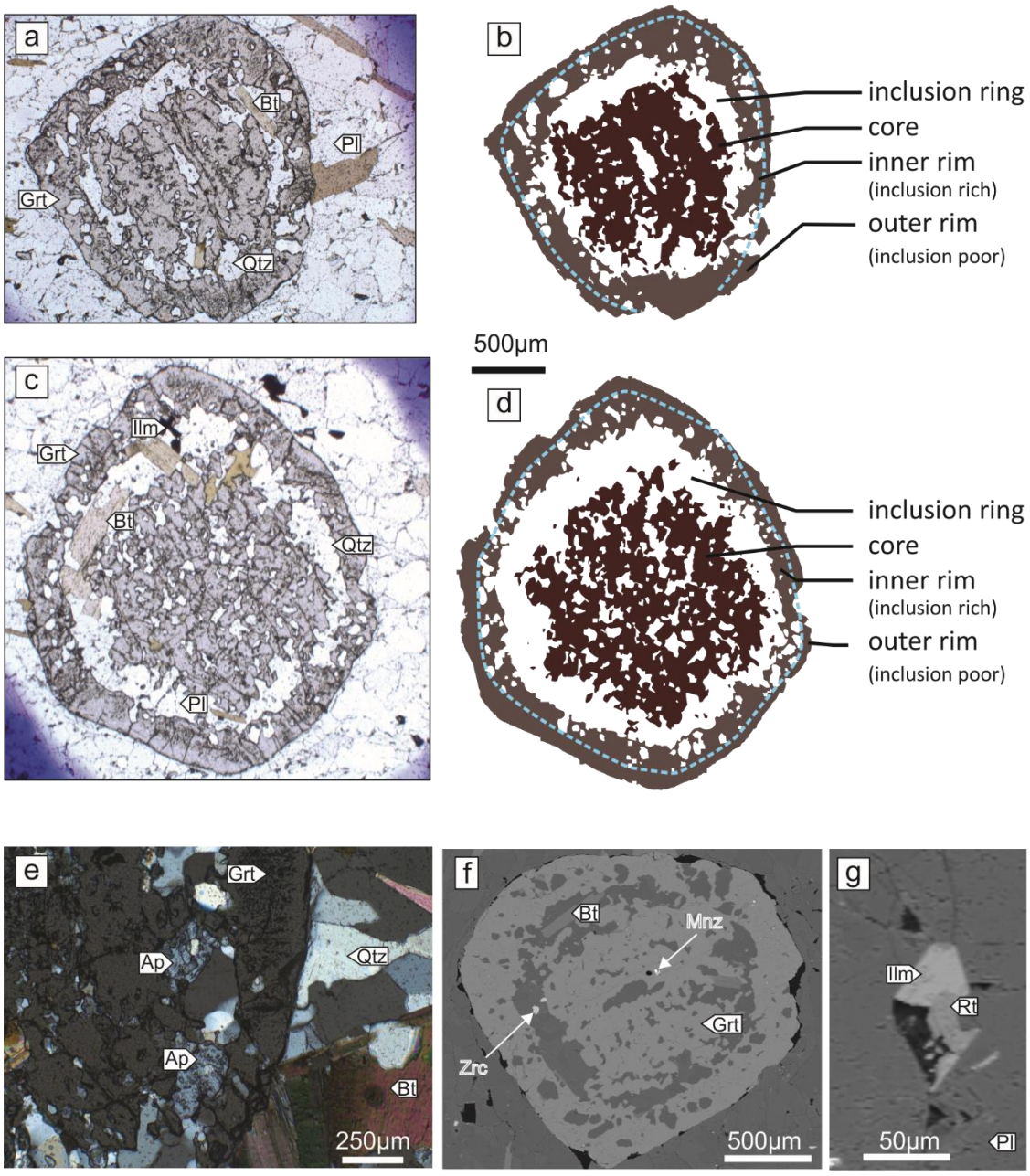

623

624 **Figure 2.** Garnet textural relationships. (a-d) Representative garnet textural domains.

625 Both porphyroblasts shown contain a poikiloblastic core, a polymineralic inclusion ring,

626 an inclusion-rich inner core, and a thin inclusion-poor outer rim; (e) Apatite in garnet

627 inclusion ring; (f) Monazite and zircon inclusions in garnet; (g) Ilmenite overgrowing

rutile in the matrix. Abbreviations: Ap = apatite; Bt = biotite; Grt = garnet; Ilm = ilmenite; Mnz = monazite; Pl = plagioclase; Rt = rutile; Qtz = quartz; Zrc = zircon.

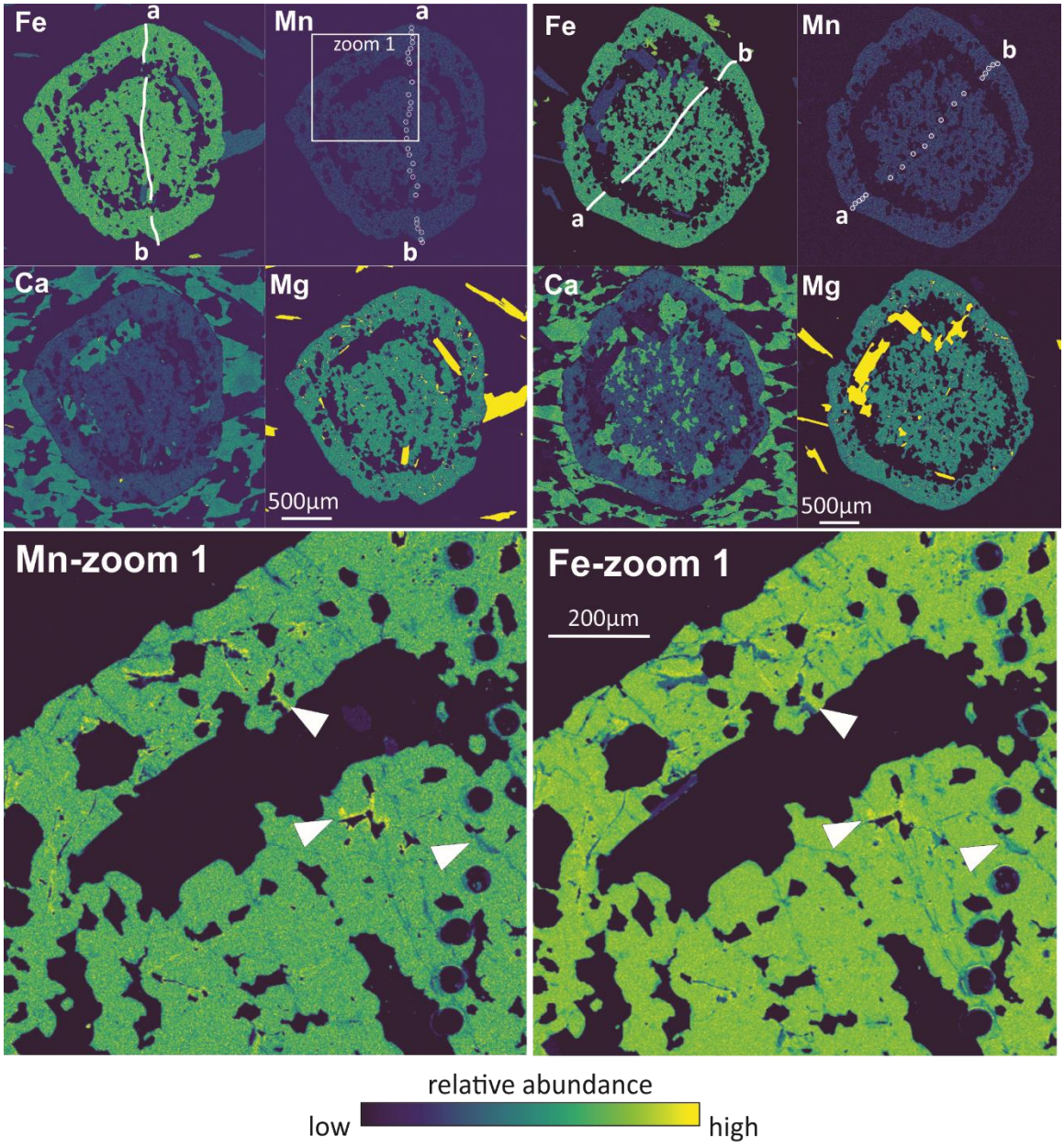

Figure 3. Garnet major element chemistry. Qualitative EPMA X-ray maps.

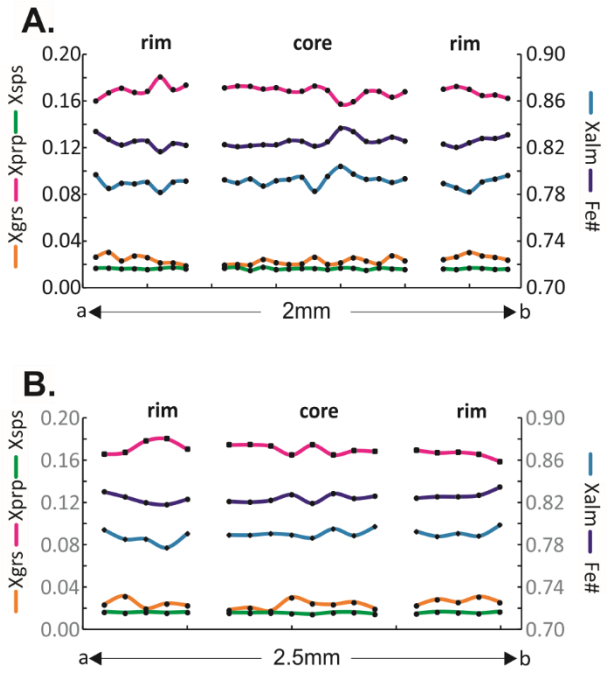

632

633 **Figure 4.** Quantitative EPMA spot transects. A-B are garnets 1 and 2 respectively. The

634 locations are shown on figure 3. Data are provided as supporting material (Table S2).

635

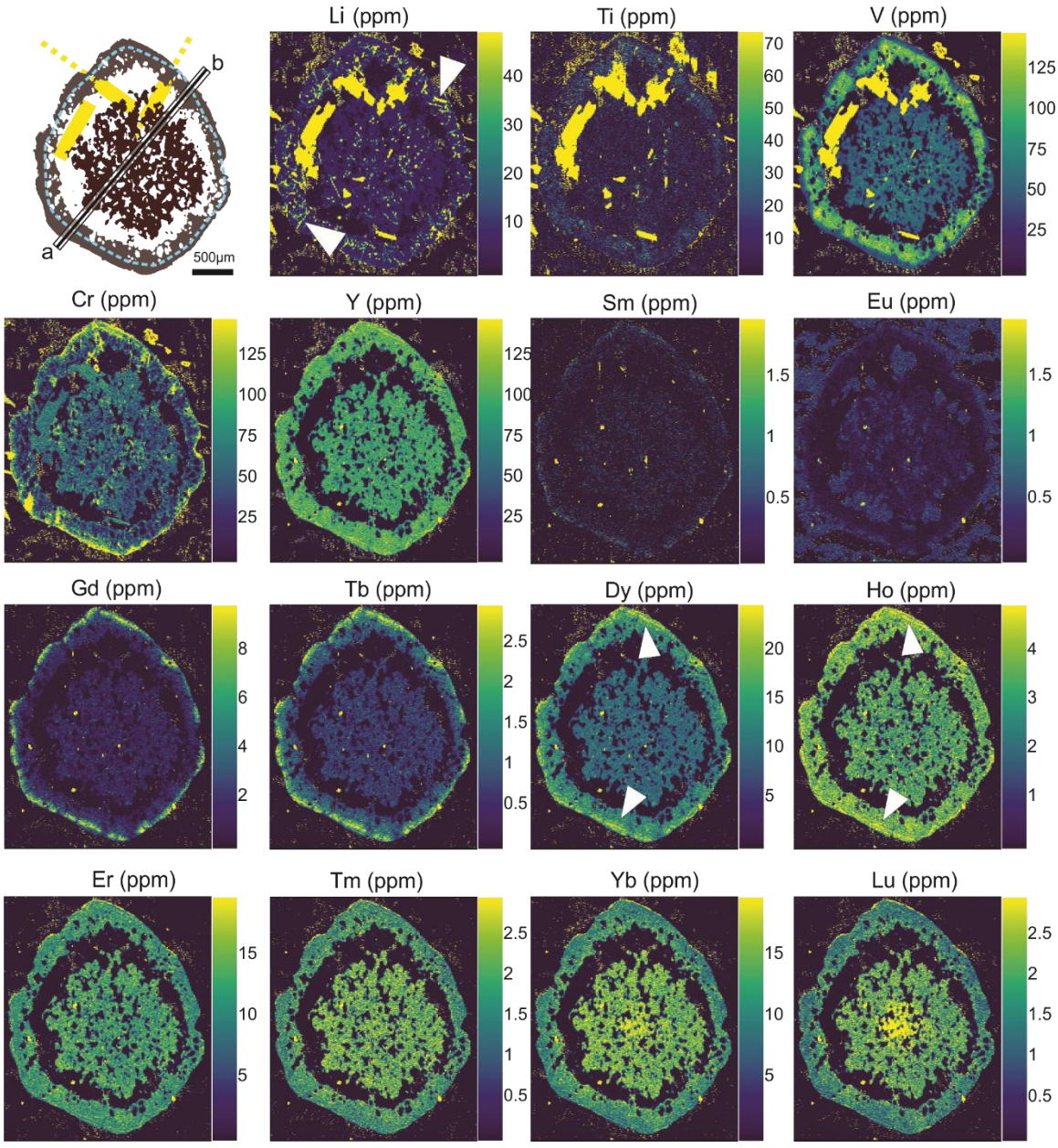

636

637 **Figure 5.** Garnet trace element distribution illustrated by selected quantified LA-ICP-MS

638 maps. The orientation of the two schistosity plans (yellow dashed lines) and the location

639 of the 1D profile presented in Figure 6 are indicated on the top-left panel.

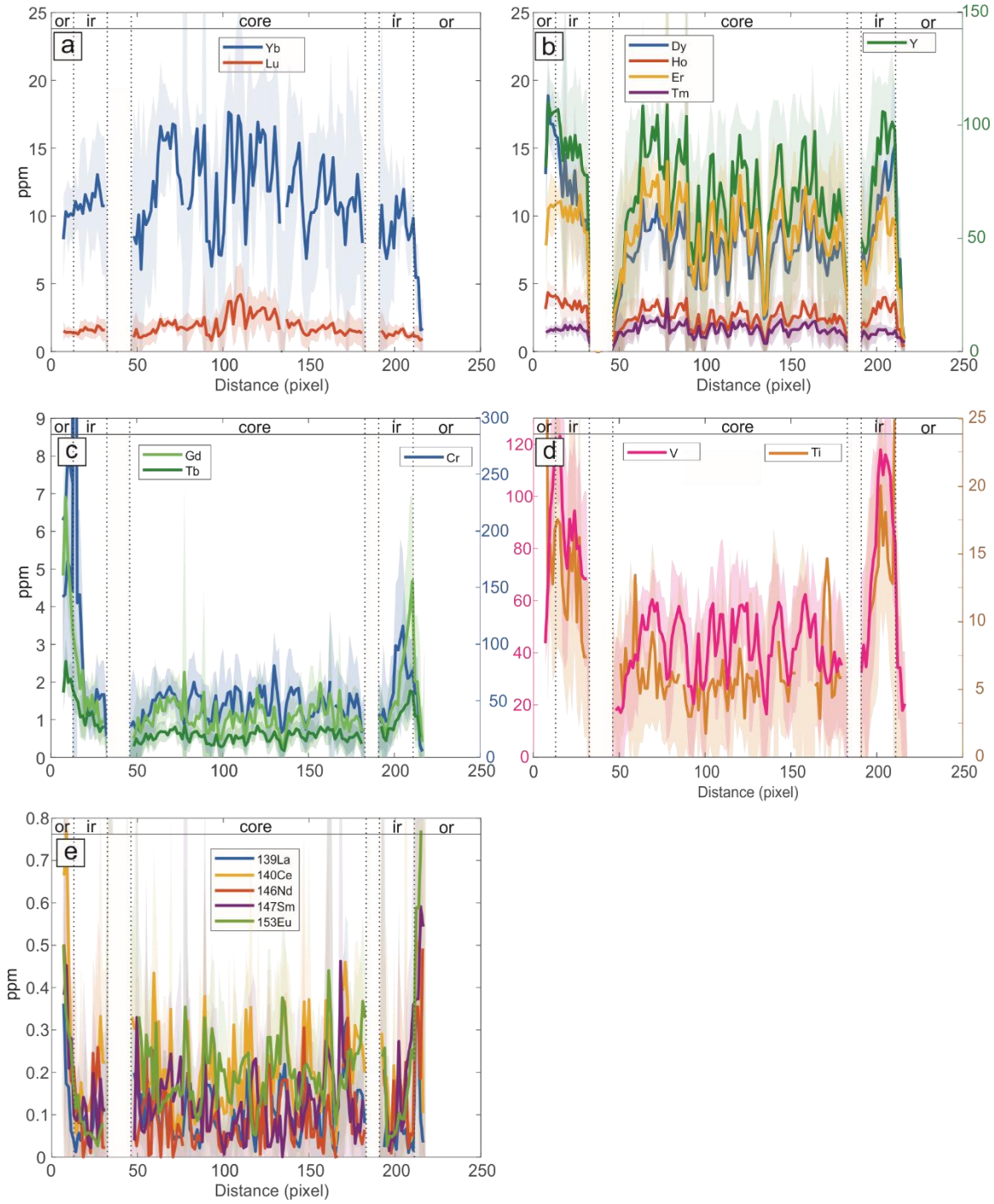

640

641 **Figure 6.** Quantified 1D profiles across the garnet grain (mean values, 2 SD contours),
642 extracted from the stitched raster data using the XMapTools strip line mode sampling
643 function (Raimondo et al., 2017). See Fig. 5 for profile location. Abbreviations: ir = inner
644 rim; or = outer rim.

645 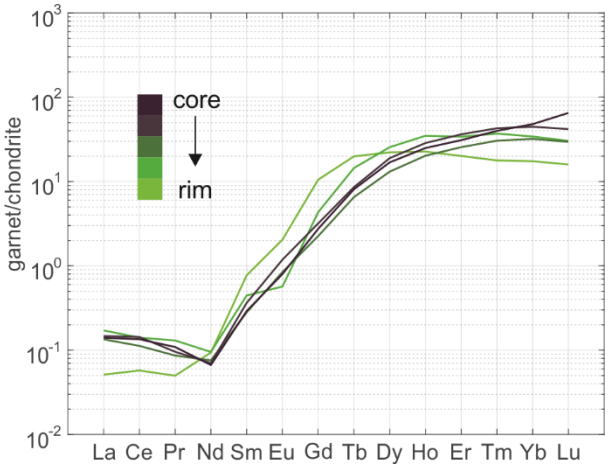

646 **Figure 7.** Chondrite-normalized REE diagram indicating the change in HREE slope from
647 core (purple) to rim (green). Chondrite normalization follows Taylor and McClennan
648 (1985).

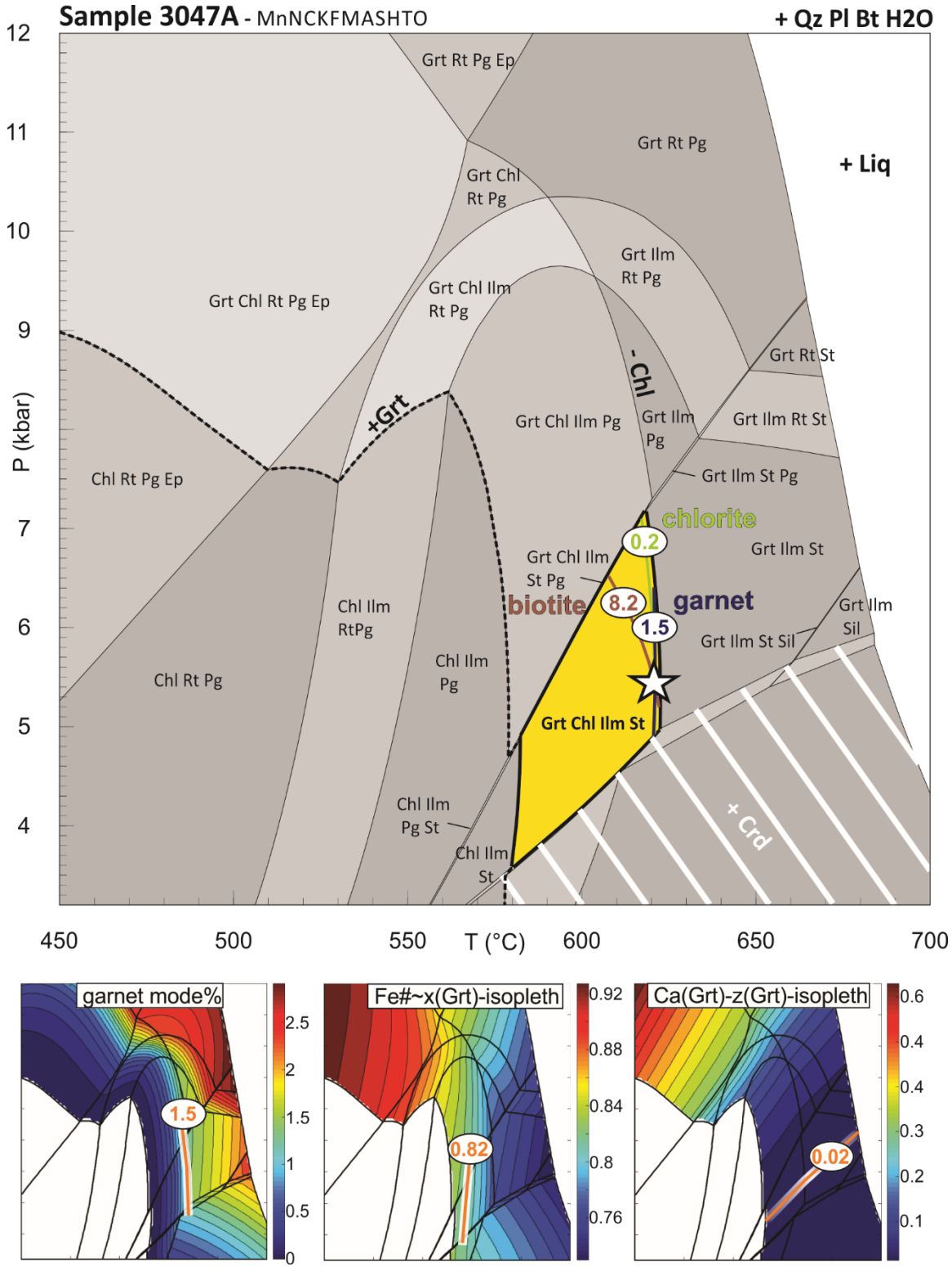

649

650 **Figure 8.** P-T pseudosection after Godet et al. (2020b), with contoured garnet and

651 plagioclase isomodes and isopleths (x(Grt) = Fe# = $Fe^{2+}/(Fe^{2+}+Mg^{2})$); z(Grt) = XCa =

652 $Ca^{2+}/(Ca^{2+}+Fe^{2+}+Mg^{2+})$. The yellow field highlights the assemblage of interest. Modelled

653 modal proportions of rock forming minerals including garnet, biotite, and chlorite are

654 shown. The white star indicates the interpreted peak conditions.

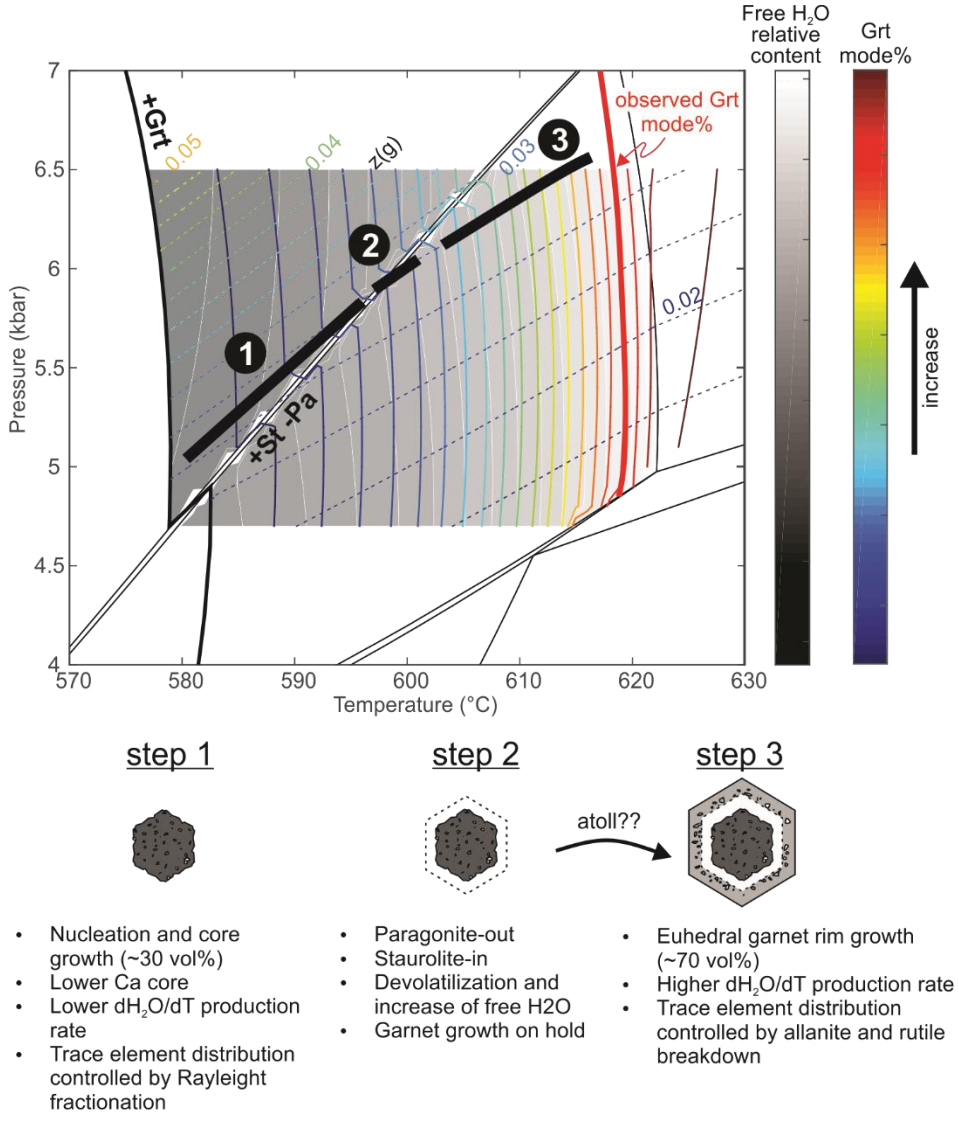

655

656 Figure 9: Schematic growth history of atoll-garnet along a prograde P-T path as discussed

657 in text. The grey level bar scale represents the free H_2O relative content, the color bar

scale shows the relative modal proportion of garnet, and the color dashed lines show the grossular content (z(g)) in garnet.